https://www.aimspress.com/journal/Materials

Research article

Effect of Yttrium on corrosion resistance of Zr-based alloys in Ringer's lactate solution for biomaterial applications

Muhammad Awwaluddin[1,2,*], Sri Hastuty[3,*], Djoko Hadi Prajitno[4], Makmuri[1], Budi Prasetiyo[1], Yudi Irawadi[1], Jekki Hendrawan[5], Harry Purnama[5] and Eko Agus Nugroho[5]

[1] Research Center for Structural Strength Technology, National Research and Innovation Agency, Tangerang Selatan 15310, Indonesia

[2] Department of Mechanical Engineering, Faculty of Engineering, Universitas Pamulang 15314, Indonesia

[3] Department of Mechanical Engineering, Faculty of Industrial Technology, Universitas Pertamina, Jakarta 12220, Indonesia

[4] Research Center for Radiation Process Technology, National Research and Innovation Agency, Bandung 40111, Indonesia

[5] Research Organization of Energy and Manufacturing, National Research and Innovation Agency, Indonesia

* **Correspondence:** Email: muha112@brin.go.id, sri.hastuty@universitaspertamina.ac.id.

Abstract: In this study, several types of zirconium-based alloys supplemented with 2, 3, and 4, in wt.% of yttrium for corrosion resistance enhancement were investigated. The specimens were prepared by a single arc welding furnace in an argon-controlled atmosphere. By optical and scanning electron microscopy, energy dispersive spectroscopy, X-ray diffraction, and electrochemical tests, the effect of different portions of yttrium on the surface morphology, phase structure, and corrosion resistance in the Zr alloys were analyzed. As of result of arc welding, the specimens were obtained and examined by optical microscope and then homogenous structures were observed. These structures are matrix (Zr-rich) and oxides. Furthermore, as of the characterization results by X-ray diffraction, the main compound of the alloys was Zr6Mo6AlTi, while others were $AlZr_3$, MoO_2, ZrO_2, and Y_2O_3 oxides. Yttrium addition in the alloys prior to the corrosion test led to thickened grain boundaries but reduced grain size. The Y_2O_3 itself remained at the grain boundaries as clusters. The corrosion test was performed in Ringer's lactate solution by using anodic polarization. The effect of yttrium addition into Zr-based alloys was found to be beneficial by shifting the corrosion potential toward a positive value. Zr-6Mo-6Al-Ti-4Y

had a higher open corrosion potential value than the other two alloys. The difference was approximately 200 mV. However, the passive region of Zr-6Mo-6Al-Ti-4Y was the shortest and broke down at an earlier stage. The formation of these kinds of oxides was the reason for the increase in corrosion potential of Zr-based alloys with 4% Y added.

1. Introduction

Recently, the development of biomaterials for bone implants has gained significant attention in the medical industry. The selected materials range from light metals, such as magnesium, to higher atomic number materials, such as stainless steel and titanium. However, only a few of them have been investigated for bone plate applications due to the number of requirements that must be fulfilled by the materials. First, the biomaterials must have excellent biocompatibility, not exhibiting adverse reactions to the body and its tissues [1–3]. Second, they must have high mechanical strength and excellent corrosion resistance in body fluids [4–6]. Finally, they must have a low elastic modulus (that of the natural human bone is 15–30 GPa) [7].

Zirconium and its alloys have attracted attention as candidates for bone implants [8]. They are also bioactive materials with very good biocompatibility [9] as they can form apatite layers like bone on the surface of living creatures [10]. Elemental zirconium itself appears to be non-toxic and non-allergenic [11–15]. In general, Zr shows high mechanical strength, high toughness to fracture [9], and low elastic modulus: approximately 60 GPa in β phase and 100 GPa in α phase [16,17]. Besides that, Zr has good corrosion resistance to application for biomaterial knee implant components [9,10,18]; thus, it can function as a bone plate material. For that reason, Zr-based alloys have recently been used as orthopedic biomaterials [19,20]. As a result, Zr alloys have become an ideal material to be developed as bone plates to replace biological hard tissues. However, applying Zr alloys to hard tissues such as bone plates is rarely done.

Zr has two crystal lattice structures; at low temperatures, it will form an α phase with a hexagonal close-packed crystal structure (HCP), while at high temperatures, it will form a β phase with a body-centered cubic (BCC) crystal structure. This structure transformation takes place at approximately 863 °C but can be modified by the addition of other elements [17,21]. In the β phase, the grain boundaries of the alloy are visible, while in the α phase the grain boundaries look relatively thin. Further studies to enhance the mechanical stability of Zr alloys are being progressively undertaken with the addition of molybdenum, niobium, aluminum, titanium, and yttrium.

Molybdenum has been added to the Zr alloy to stabilize the Zr alloy phase, also reducing cytotoxicity and magnetic susceptibility [22,23]. The microstructure and magnetic susceptibility of Zr-Mo alloys have been used for body implants to minimize the effect of magnetic resonance imaging (MRI) [7,22,24]. Further, it has also been proposed to create binary alloys, low modulus, and a strengthening effect [25–29]. Ti and Al were also added to increase material inertness and corrosion resistance [30–34]. Yet, the role of yttrium is not well known, although being thought to increase the corrosion resistance of Zr alloys, as reported for Fe alloys [35].

In this paper, the alloy biomaterial Zr-6Mo-6Al-Ti-xY is designed with an yttrium content of 0%, 2%, 3%, and 4%. The effect of the combination of additional elements with Zr is essential knowledge to develop potential biomaterials with outstanding corrosion performance for bone implants.

2. Material and methods

2.1. Sample preparation

The raw materials consisted of 99% pure zirconium sponge (Aldrich Chemical), 99.8% pure molybdenum rod (Goodfellow), 99.9% pure aluminum (INALUM), 99.9% pure titanium and yttrium, and Otsu-RL Ringer's lactate solution (PT Otsuka Indonesia). The metals were weighed to a total mass of 15 g of each sample using a Mettler Toledo AL204 analytical balance by following the composition shown in Table 1.

Table 1. Chemical composition of Zr-based alloys (in wt.%).

Composition alloy	Zr		Mo		Al		Ti		Y	
(as cast)	wt.%	g	wt.%	g	wt.%	g	wt.%	g	wt.%	g
Zr-6Mo-6Al-1Ti	87	13.05	6	0.9	6	0.9	1	0.15	-	-
Zr-6Mo-6Al-1Ti-2Y	85	12.76	6	0.9	6	0.9	1	0.15	2	0.30
Zr-6Mo-6Al-1Ti-3Y	84	12.58	6	0.9	6	0.9	1	0.15	3	0.45
Zr-6Mo-6Al-1Ti-4Y	83	12.45	6	0.9	6	0.9	1	0.15	4	0.60

The process continued with the melting of all metals in a single arc melting furnace. A tungsten electrode was used as the heating element with an electric current of 120 A and an applied voltage of 230 V. The furnace was given a flow of high-purity argon gas (99.99%) to protect the melted metals from oxidation. The samples were melted six times to produce a homogenous structure. The final specimens were 2 cm in diameter and 0.4 cm in thickness.

2.2. Characterization

The samples were prepared for metallographic examination by grinding using SiC sandpaper of up to 2000 grade. Afterward, the process continued with polishing. ZrO_2 powder was used as abrasive particle. As for the etching process, a solution of 5% H_2SO_4, 10% HF, 30% HNO_3, and 55% H_2O was prepared. Characterizations of the new alloys were done by using an Olympus BX51 optical microscope (OM), JEOL JSM-6510LA, and a Jeol JSM-IT200 scanning electron microscope (SEM) to analyze grain size and boundaries, and an energy-dispersive spectroscopy (EDS) equipment to analyze the composition and homogeneity of the alloys. The X-ray diffraction patterns for the Zr-6Mo-6Al-Ti-xY (x = 0, 2, 3, and 4 wt.%) alloys were characterized using an X-ray diffractometer, namely PANalytical XPert Pro, where the X-ray tube had a CoKα wavelength = 1.7889 Å and step size of 0.02°. The Rietveld method available with GSAS software was utilized to analyze the peak data or X-ray diffraction profiles, including lattice parameters, mass fraction, unit cell volume, and atomic density.

2.3. Corrosion tests

In the test, Ringer's lactate solution at 37 °C was used to cathodically and anodically polarize the test specimens of Zr-6Mo-6Al-Ti-xY. The testing employed a three-electrode configuration consisting of working, counter, and reference electrodes. The specimens served as the cathode, while the anode was formed by a platinum wire of 0.5 mm diameter and the reference electrode was formed by silver-silver chloride (SSE) or Ag-AgCl in saturated KCl solution. Corrosion resistance measurements were performed with an Autolab Potentiostat GS304. The applied potential was between −1.5 V and 1 V with a scan rate of 1 mV/s.

Table 1 presents the chemical composition of the Zr-based alloys used in this study. The number before the element indicates the weight percentage of that element, while zirconium is the balance element. The yttrium serves as the independent variable in this experiment.

Table 2 displays the chemical composition of Ringer's lactate solution utilized as the simulated body fluid. The main component is sodium chloride.

Table 2. Chemical composition of Ringer's lactate solution.

Reagent	Composition (g/mL)
Calcium chloride dihydrate	0.10 g
Sodium chloride	3.00 g
Potassium chloride	0.15 g
Sodium lactate	1.55 g
Lactate (HCO_3^-)	28 mEq/L
Sodium	130 mEq/L
Calcium	2.7 mEq/L
Potassium	4 mEq/L
Chloride	108.7 mEq/L
Water for injection	ad 500 mL
Osmolarity	273 mOsm/L
K^+	4 mEq/L
Na^+	130.3 mEq/L

3. Results and discussion

The optical observation of the etched surface of Zr-based alloys with or without Y added can be observed in Figure 1. Figure 1a displays the microstructure of Zr-based alloy without Y addition; an average 101.6 µm diameter of equiaxed grains and a standard deviation of 43.7 µm are observed. However, the grain boundary is not clear. In Figure 1b, regarding the Zr alloy with 2 wt.% of Y, the equiaxed grains are separated by bold and vivid boundaries, with an average of 38 µm and a standard deviation of 9.7 µm. A similar observation is found in Zr alloys with 3 and 4 wt.% of Y (Figure 1c,d); an average 29.8 and 19.4 µm equiaxed grains with a standard deviation of 7.9 and 1.9 µm, respectively. From Figure 1a to 1d, it is visible that the grain size of the samples is decreasing. It is thought that the Y addition plays a significant role in forming this structure.
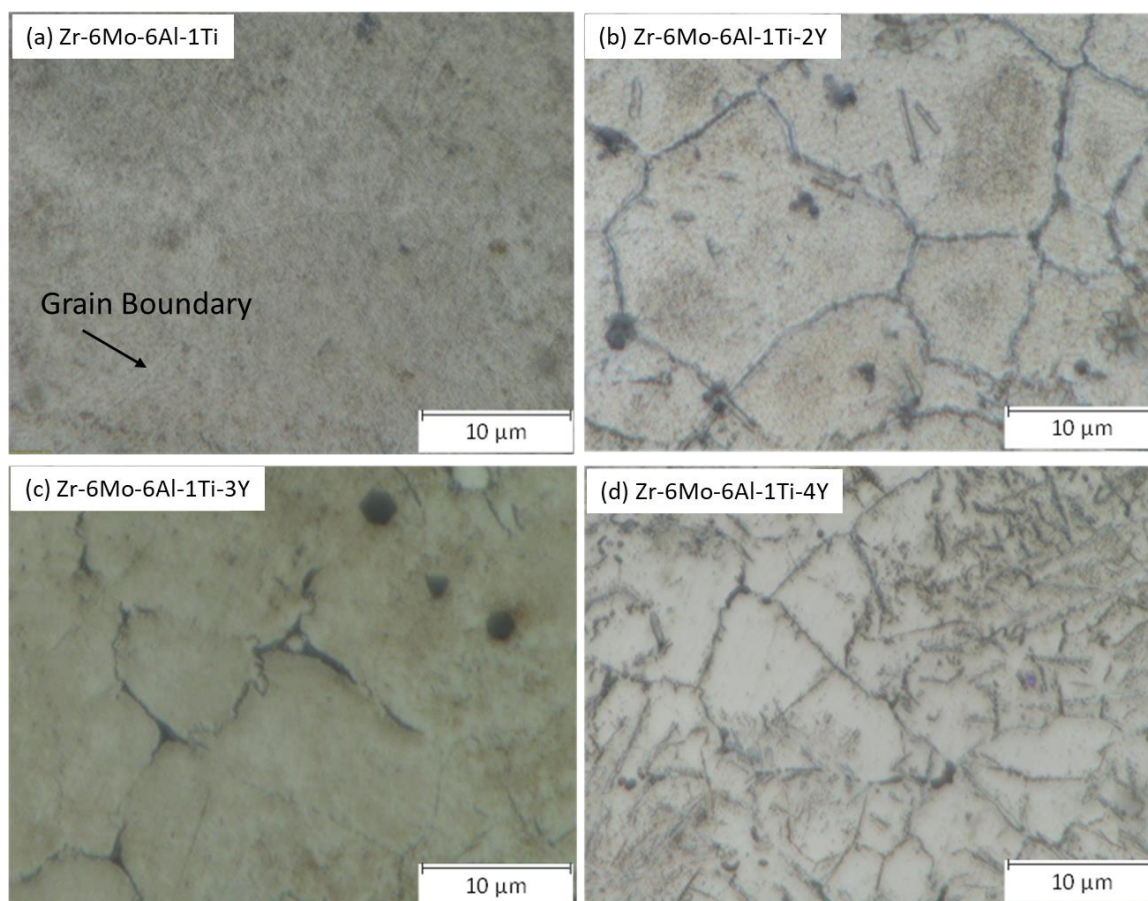
Figure 1. Optical observation of Zr-based alloys: (a) Zr-6Mo-6Al-1Ti; (b) Zr-6Mo-6Al-1Ti-2Y; (c) Zr-6Mo-6Al-1Ti-3Y; (d) Zr-6Mo-6Al-1Ti-4Y.

The results of SEM observation of Zr alloys with 0, 2, 3, and 4 wt.% of Y are displayed in Figure 2. The matrix and grain boundaries are shown by arrows. These figures confirmed the results of optical observation. In addition, clusters of the second phase are spotted at the grain boundaries of 2–4 wt.% of Y. These figures confirmed the results of the previous Figure 1: Increasing the weight percentage of Y makes visible grain boundaries.
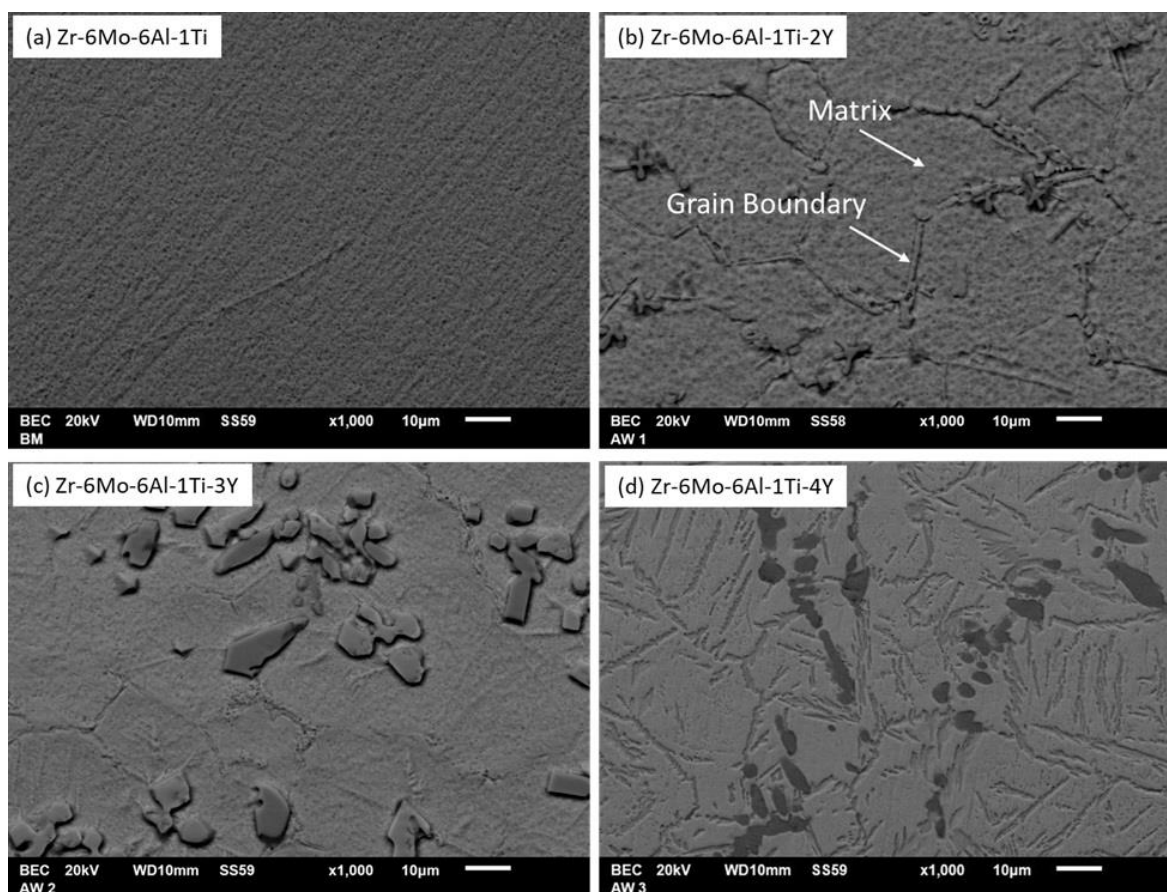
Figure 2. SEM morphologies of Zr-based alloys after etching prior to corrosion test: (a) Zr-6Mo-6Al-1Ti; (b) Zr-6Mo-6Al-1Ti-2Y; (c) Zr-6Mo-6Al-1Ti-3Y; (d) Zr-6Mo-6Al-1Ti-4Y.

Figure 3 shows microscopic SEM images after the corrosion test in Ringer's lactate solution. Figure 3a represents the Zr-6Mo-6Al-Ti surface, displaying a clean surface with few dark particles. Figure 3b represents the Zr-6Mo-6Al-Ti-2Y surface, with finer grain boundaries and the presence of other phases, with scattered dark and gray spots at the grain boundaries. Figure 3c represents Zr alloys with 3 wt.% of Y. As displayed, the grain boundary lines get finer and thinner, and the dark and gray spots get larger. In Figure 3d, regarding Zr alloys with 4 wt.% of Y, the grain boundaries are not seen clearly and seem to have disappeared. On the other hand, the number of gray spots increased and formed clusters. From these photographs, it seems that the addition of Y promotes the disappearance of grain boundaries and increases the density of gray spots at the grain boundaries.

Further characterizations were done to identify the chemical composition of the matrix and other phases appearing in the surface photographs. These characterization methods were electron dispersive spectroscopy (EDS) mapping and X-ray diffraction (XRD).
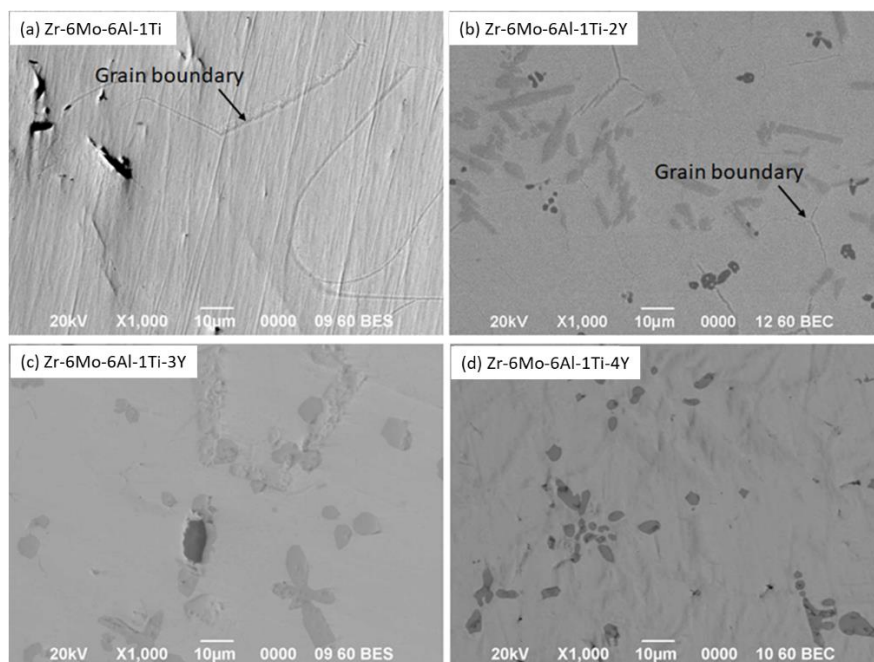
Figure 3. SEM morphologies of Zr-based alloys after corrosion test: (a) Zr-6Mo-6Al-1Ti; (b) Zr-6Mo-6Al-1Ti-2Y; (c) Zr-6Mo-6Al-1Ti-3Y; (d) Zr-6Mo-6Al-1Ti-4Y.
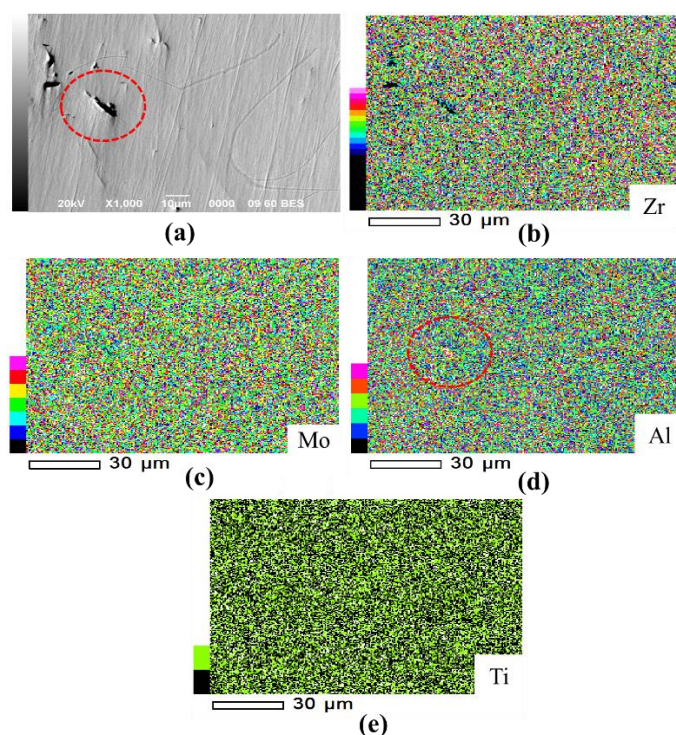

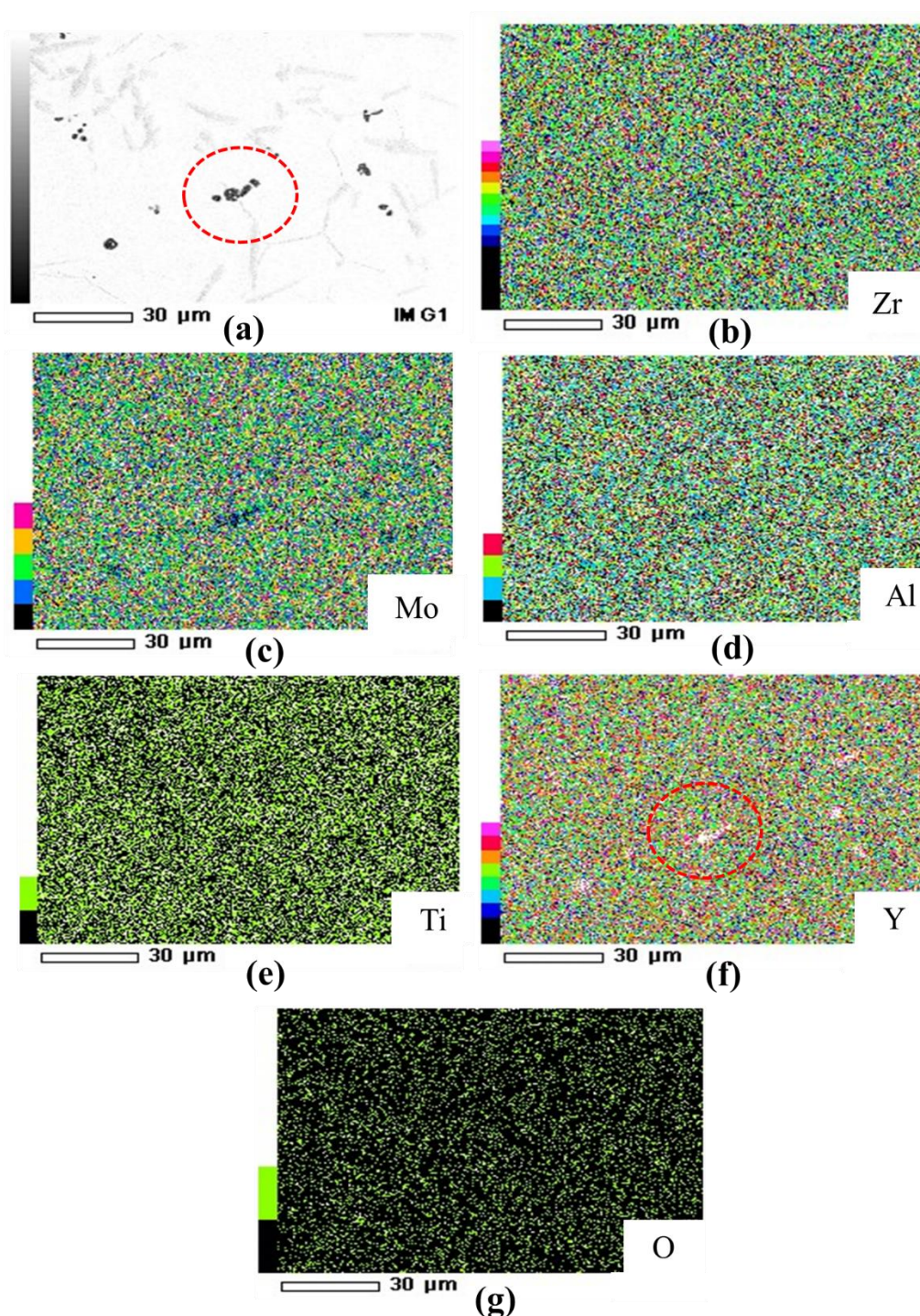**Figure 4.** Elemental mapping of corroded surface of Zr-6Mo-6Al-1Ti.

Figure 4 shows the elemental mapping of corroded surface of Zr-6Mo-6Al-1Ti alloy. In Figure 4a shows the observed area of Zr, Mo, Al, and Ti distribution in Zr-6Mo-6Al-1Ti alloy after the corrosion test. Figure 4 b–e shows the distribution of Zr, Mo, Al, and Ti in the area: the matrix is covered uniformly. Figure 4d shows the distribution of the element Al in the area, with the circle

highlighting aluminum oxide (Al_2O_3). It seems that Al was not completely dissolved in the Zr matrix and formed Al_2O_3.
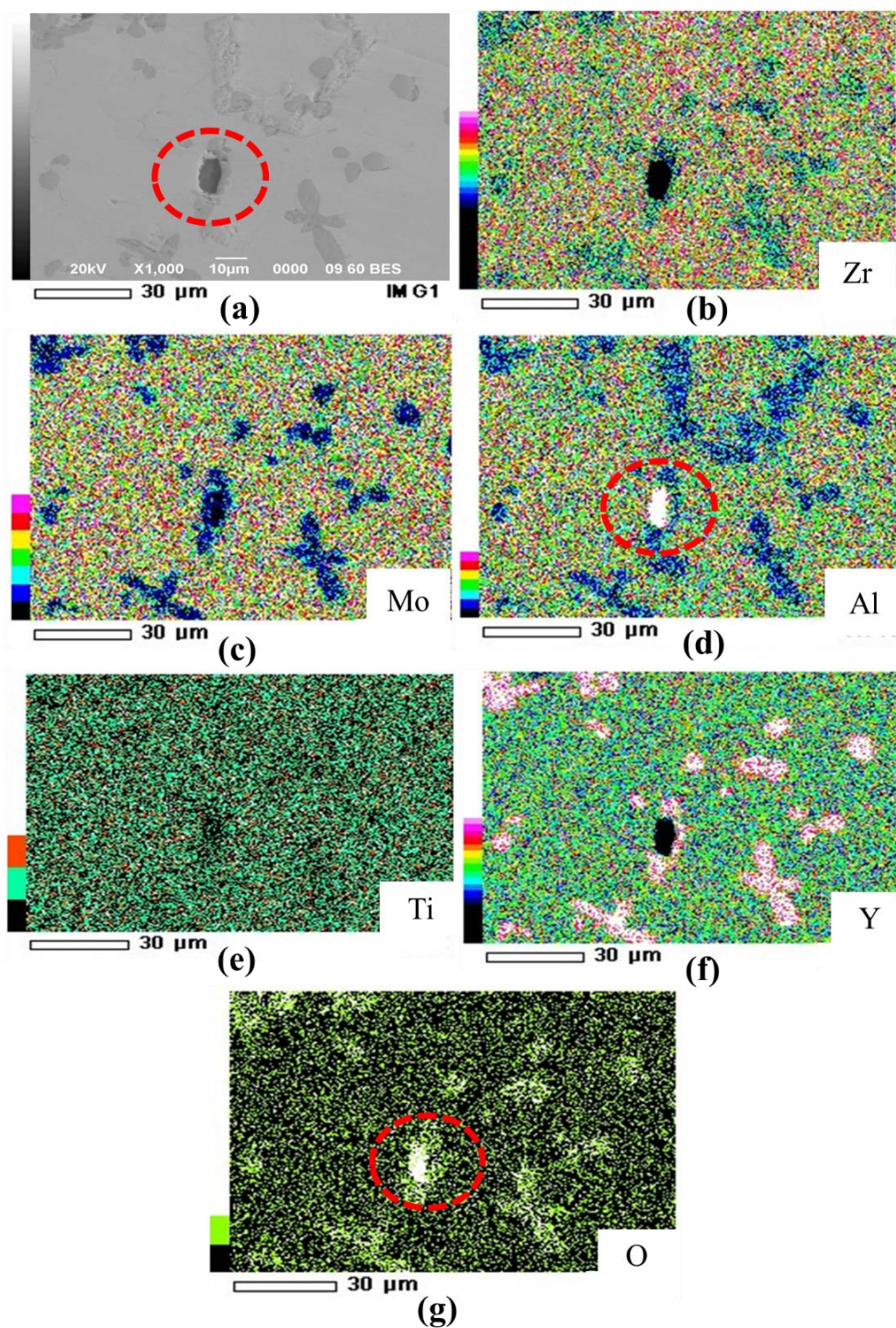

Figure 5. Elemental mapping of the corroded surface of Zr-6Mo-6Al-1Ti-2Y.

Figure 5 shows the elemental mapping of the corroded surface of Zr-6Mo-6Al-1Ti-2Y alloy. In Figure 5 a–g shows the area of distribution of Zr, Mo, Al, Ti, Y, and O in Zr-6Mo-6Al-1Ti-2Y alloy. The dark particles on the circle are yttrium oxide (Y_2O_3) (Figure 5a,f). This type of oxide was not

incorporated with other elements in the alloys. Another oxide was also found, in the form of flakes, which is characterized as zirconium oxide, ZrO_2.
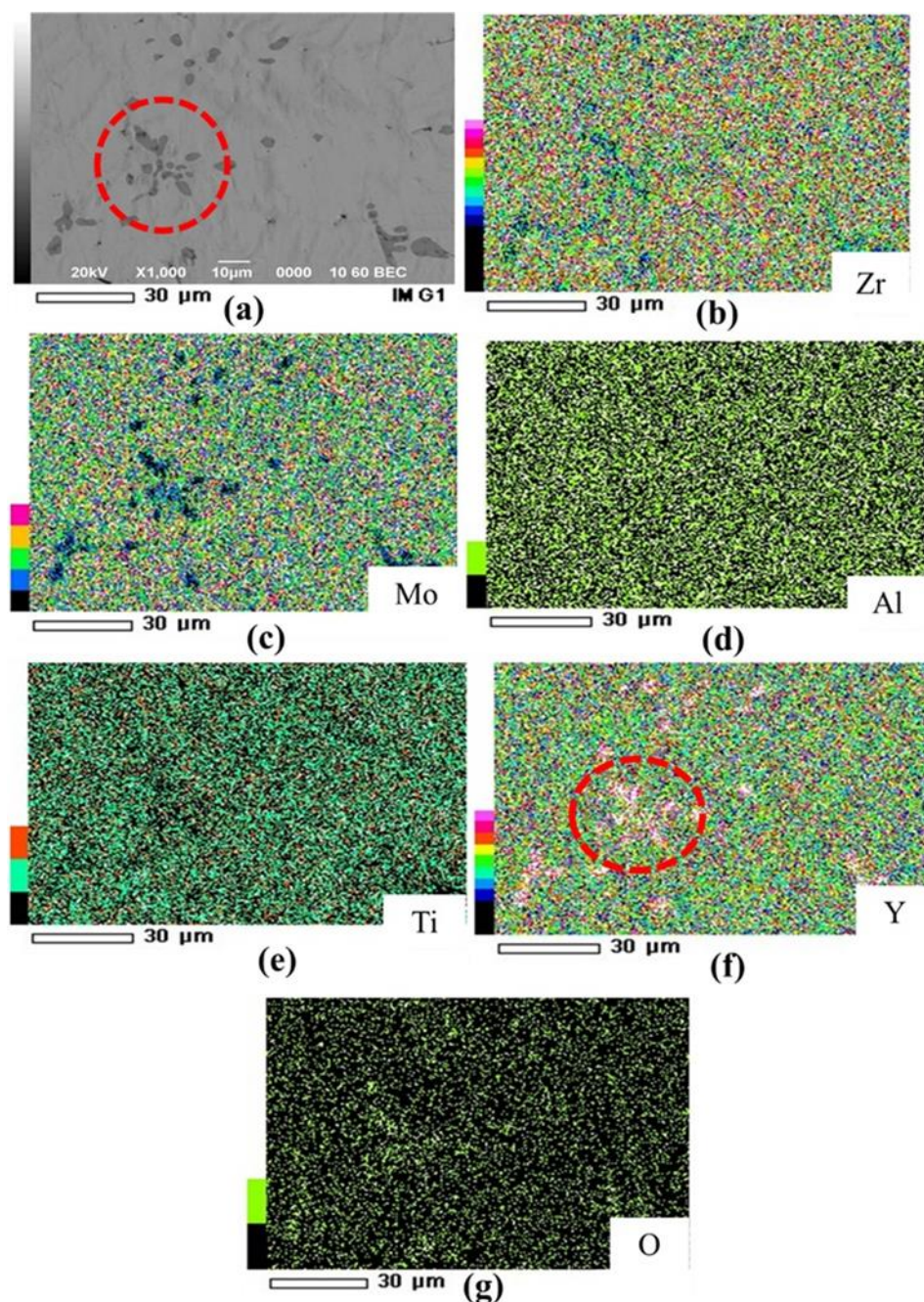

Figure 6. Elemental mapping of corroded surface of Zr-6Mo-6Al-1Ti-3Y.

Figure 6 shows the elemental mapping of corroded surface of Zr-6Mo-6Al-1Ti-3Y alloy. In Figure 6 a–g shows the area of the distribution of Zr, Mo, Al, Ti, Y and O in Zr-6Mo-6Al-1Ti-3Y

alloy. By increasing the yttrium content in the alloys by 3 wt.%, the particle size of Al, Y, and Zr oxides also increased. In case of Al oxides, the particles reached 10 μm (Figure 6d,g). Figure 6f shows that yttrium forms clusters but is evenly distributed on all surfaces.

Figure 7. Elemental mapping of corroded surface of Zr-6Mo-6Al-1Ti-4Y.

Figure 7 shows the elemental mapping of corroded surface of Zr-6Mo-6Al-1Ti-4Y alloy. In Figure 7 a–g shows the area of the distribution of Zr, Mo, Al, Ti, Y and O in Zr-6Mo-6Al-1Ti-4Y alloys, where the appearance of clustered yttrium oxides is still clearly seen. The presence of Y_2O_3 stands alone in the Zr matrix (Figure 7f), not consolidated with Mo, Ti, and Al. Furthermore, Mo

exists in the matrix in the form of MoO_2, molybdenum oxide, with its presence distributed uniformly on the surface.

In order to confirm the chemical composition of the alloys, X-ray diffraction characterization was carried out. The black, red, blue, and red lines represent Zr alloy with 0, 2, 3, and 4 wt.% of Y, respectively. From this characterization, it was found that these alloys formed Zr compounds, Zr-6Mo-6Al-1Ti-xY, $AlZr_3$, ZrO_2, and MoO_2.
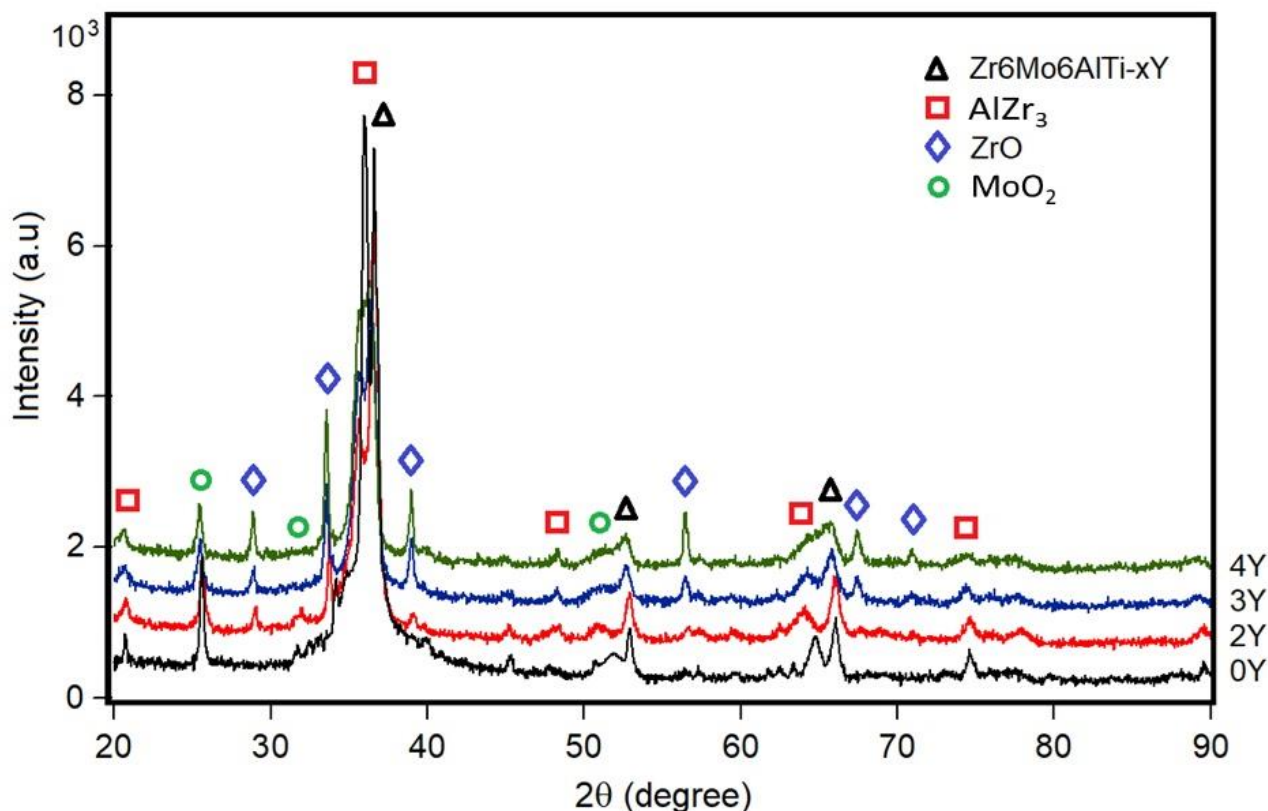

Figure 8. X-ray diffraction patterns of Zr-6Mo-6Al-Ti-xY.

Figure 8 shows the X-ray diffraction pattern of the Zr-6Mo-6Al-Ti-xY alloy. The XRD patterns in black, red, blue, and green represent Zr-6Mo-6Al-Ti-x alloys with the x composition of 0, 2, 3, and 4 wt.% Y, respectively. It appears that all alloy compositions have successfully formed the Zr6Mo6AlTi-xY phase cubically structured with the space group Im-3m. In addition, several phases were found, which are suspected to be the results of imperfection reactions and the oxidation that occurred during the melting process. These phases were $AlZr_3$, ZrO_2, and MoO_2, analyzed quantitatively based on the Rietveld method using the general structure analysis system (GSAS) with the fitting parameters according to Toby et al. [36]. Meanwhile, the phases were identified by referring to the American Mineralogist Crystal Structure Database (AMCSD) and the Crystallography Open Database (COD). The structures of $AlZr_3$, ZrO_2, and MoO_2 phases were cubic (space group Pm-3m), cubic (space group Fm-3m), and monoclinic (space group P1 21 / c 1), respectively. Figure 8 also shows that the peaks of the same phases are located at the same diffraction position. The analysis results showed that the mass fraction of the Zr6Mo6AlTi-xY phase increased by 55, 63, and 73 wt.% for the alloys with 2, 3, and 4 wt.% Y, respectively. However, this increase was followed by a rise of

mass fraction in the second phase, namely ZrO_2. This means that the addition of Y encourages more Zr atoms to be oxidized, while for the other second phases, the mass fraction of the $AlZr_3$ and MoO_2 phases appear to be decreasing, as shown in Figure 9.
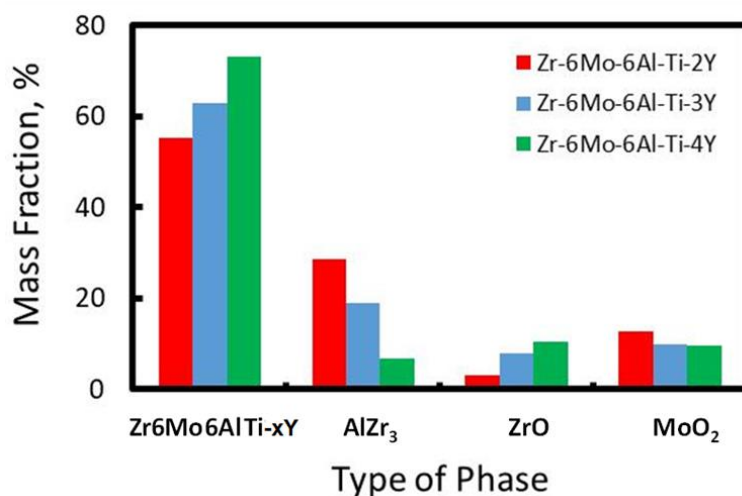

Figure 9. The mass fraction of phases of Zr-6Mo-6Al-Ti-xY.

Figure 9 shows that the main phase Zr6Mo6AlTi-xY was formed, and its mass increased with the increase in Y composition. In addition, the rise in Y composition affected the decrease of mass fraction in $AlZr_3$ phase. It is suspected that in the seven alloys, there is an excess of Zr and Mo, which will be oriented at the grain boundaries to form precipitates. Therefore, this alloy will be easily oxidized to form ZrO_2 and MoO_2. This condition is in accordance with the observation results of scanning electron microscopy (see Figures 2 and 3), which show how the oxide phase was formed on the surface of the three alloys. On the other hand, it was also found that the crystallization rate of each phase was excellent because the density values of the three alloys were relatively the same for each of the phases formed, as shown in Figure 10. The density phases of Zr6Mo6AlTi-xY, $AlZr_3$, ZrO_2, and MoO_2 for the three alloys were 5.7, 6.2, 7.6, and 5.6 g/cm^3. Therefore, the homogeneity of the alloys and the vacuum level of the synthesis instruments are of interest in the alloy-making process both before and after the argon flow.
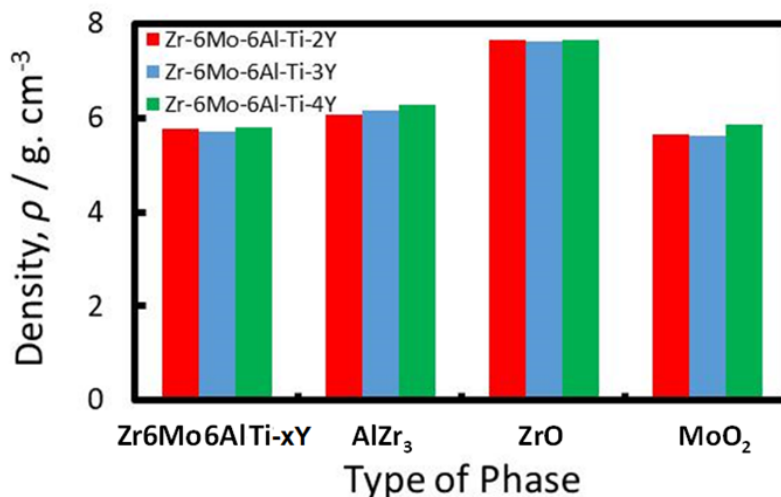
Figure 10. The density of phases of Zr-6Mo-6Al-Ti-(x)Y.

Figure 11 shows the Tafel polarization of Zr-based alloys in Ringer's lactate solution, exposing cathodic and anodic areas. In the cathodic area, the potential ranged from −1.5 V to the open-circuit potential (OCP) of each alloy. At potentials ranging from −0.9 to −0.5 V, the formation of hydroxide ions occurred. The rate of hydroxide ion formation decreased as the applied potential increased. Comparing the three alloys, the rates of cathodic reactions were all similar. As the applied potential increased, the corrosion potential (Ecorr) and current of corrosion (icorr) were reached for the three alloys, as represented by the minima in the curves in Figure 11. The Ecorr values of Zr alloys with 2Y and 3Y were quite similar, namely −0.78 and −0.83 V. For the Zr alloy with 4Y, the Ecorr value was −0.59 V, which means a difference in Ecorr of almost 200 mV. If corrosion takes place at a higher Ecorr, this indicates that the metal is more resistant to corrosion. Therefore, the Zr alloy with 4Y has a better corrosion performance than other alloys. On the other hand, the corrosion kinetic, which is represented by corrosion current, is very much the same for all alloys.
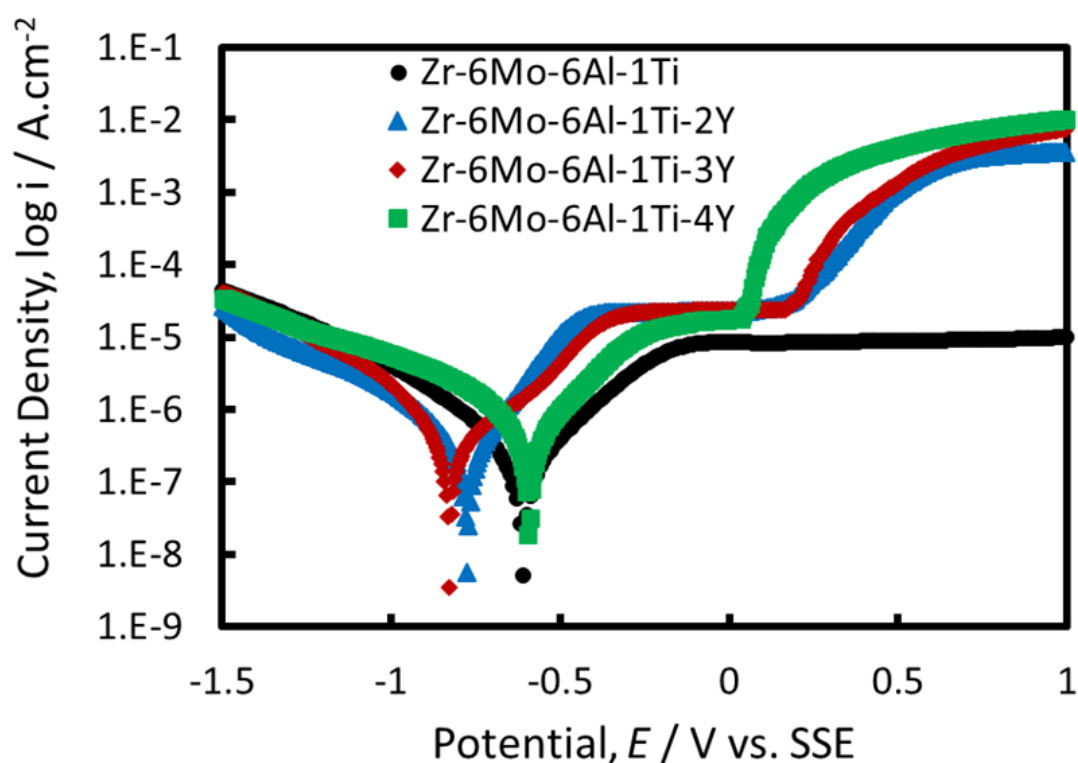
Figure 11. Tafel graph of Zr-based alloys in Ringer's lactate solution.

In Figure 12, the anodic region is divided into four distinct regions, namely active, passive, trans-passive, and secondary passivity regions. In the active region, the current density almost linearly increases, starting from the current density of corrosion (icorr). During this period, thin, dense, compact, and transparent passive films formed on the surface of alloys; the materials comprising those films are Zr6Mo6Al1Ti2Y, AlZr$_3$, MoO$_2$, and ZrO$_2$ oxide.

This phenomenon often occurs for alloys that have the characteristics of forming a passive film, such as stainless steel. The corrosion rate declines to merely $1E - 8 \log i / A. cm^{-2}$ along with the increase in potential. Further, it remains detached from the potential over a considerable potential region, known as passive region. Akimoto et al. found that Zr alloys formed rich Zr passive alloys after polarizing in chloride ion solution [37]. When the potentials increase greatly in the trans-passive region, the corrosion rate increases as well, and it is thought that the passive film breaks down. The Zr alloys with Y addition of 2 and 3 wt.% have similar breakdown potential (E$_b$) values of 0.18 and 0.17 V, respectively.
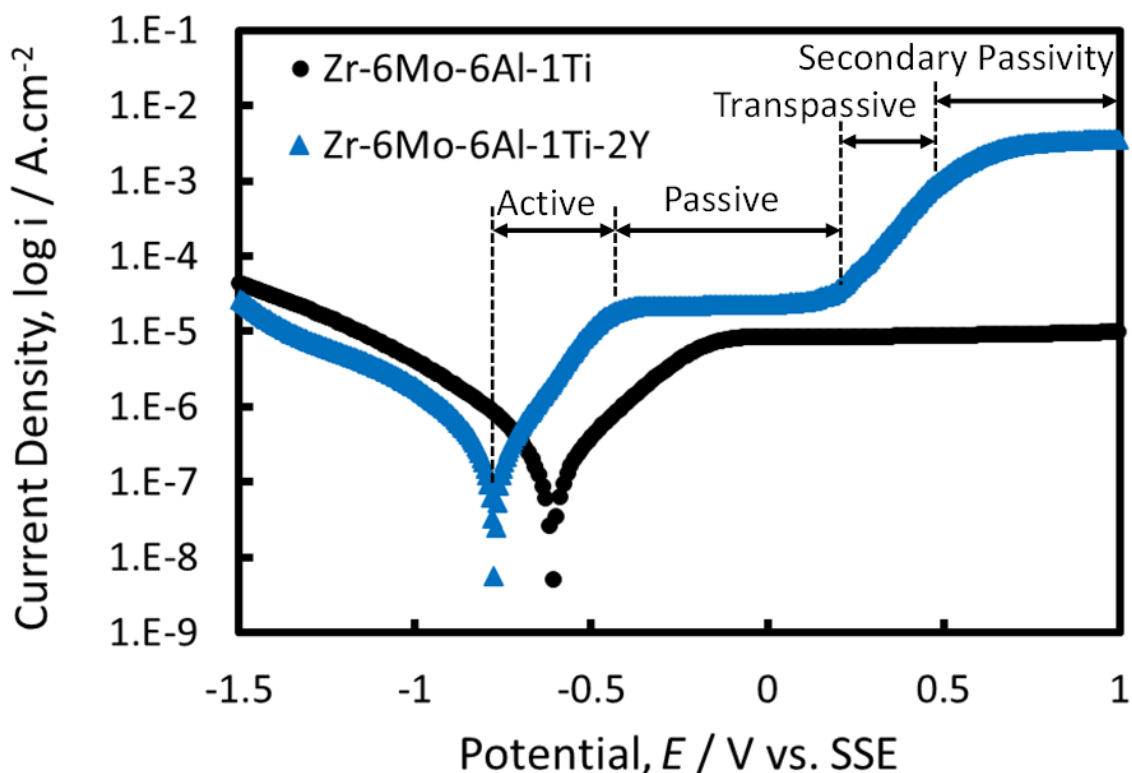
Figure 12. Classification of regions in Tafel graph of Zr-based alloys.

The Eb of the alloy with 4 wt.% of Y is 0.04 V. The value of Eb was depressed by increasing the amount of Y wt.%. The Zr alloy with 4 wt.% of Y had a thinner passive region than the 2 and 3 wt.% alloys. It is suggested that yttrium decreases the corrosion resistance and places Zr alloys at higher susceptibility to pitting. Similar results were found by L. Yu et al. [38]. It can be concluded that, as the effects of Y addition in the anodic passive and trans-passive region, OCP occurred at the higher value, and the passive film formed and broke down in the trans-passive region at an earlier stage.

Furthermore, the forward scans continued from trans-passive to secondary passivity. At this stage, the surface of Zr alloys supplemented with Y regained its passivity at higher potential. The Zr alloy without Y addition only had two regions: active and passive; the other three alloys showed four different regions: active, passive, trans-passive, and secondary passivity. The last area, secondary passivity, means that the Zr alloys with Y addition could withstand the extreme corrosion environment without significant deterioration by forming another passive layer. The Zr alloy with 4 wt.% of Y, compared with the other two alloys, showed the highest current density, which means that the formed passive film was thicker than the others.

Table 3. Electrochemical parameters of polarization for Zr alloys in aerated Ringer's lactate medium.

Alloy	Corrosion potential, E_{corr} (V)	Corrosion current, i_{corr} (A. cm^{-2})	Potential of passive film formation, E_f (V)	Potential of passive film breakdown, E_b (V)	Potential of secondary passivity, E_s (V)	E_b-E_f (V)
Zr-6Mo-6Al-1Ti	−0.69	1.58E^{-7}	−0.05	1	0	1.05
Zr-6Mo-6Al-1Ti-2Y	−0.78	1.07 E^{-7}	−0.48	0.18	0.66	0.66
Zr-6Mo-6Al-1Ti-3Y	−0.83	1.02E^{-7}	−0.38	0.17	0.4	0.55
Zr-6Mo-6Al-1Ti-4Y	−0.59	1.10E^{-7}	−0.18	0.04	0.12	0.22

The overview of electrochemical parameters of polarization for Zr alloys in aerated Ringer's lactate medium is displayed in Table 3, and the relationship of yttrium in Zr alloys with the length of passive film during anodic polarization is displayed in Figure 13.
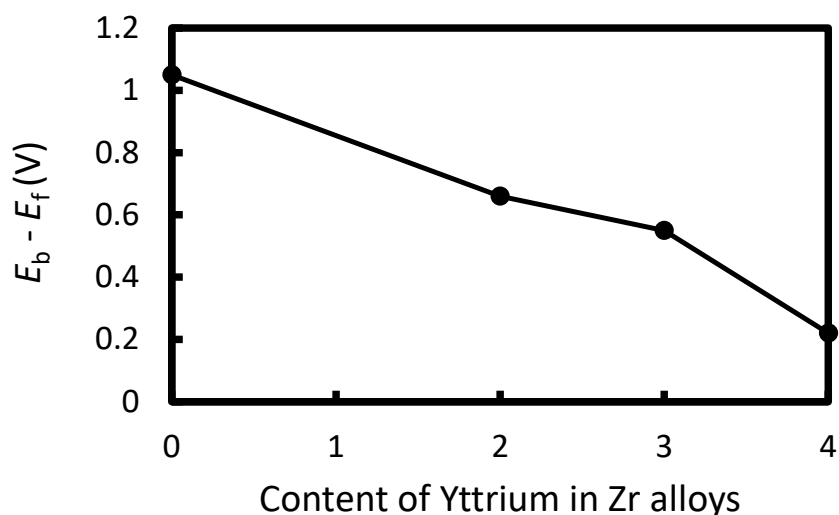

Figure 13. Relationship of content of Yttrium in Zr alloys with the length of passive film during anodic polarization.

In Figure 13, the length of passive regions, E_b-E_f, represents the ability of the alloy to hinder the corrosion. The longer the length, the more resistant is the alloy to corrosion. Figure 13 shows a trend in which the length of E_b-E_f is shorter with increased Y content, being more prone to corrosion to occur by breaking the passive film.

4. Conclusions

The fabrication and corrosion resistance of Zr-based alloys with 2, 3, and 4 wt.% of Y addition were studied. The following conclusions were drawn based on the results of this research:

1. The presence of Y in Zr alloys results in the form of yttrium oxide (Y_2O_3). This type of oxide has characteristically more visible grain boundaries. However, it has reduced grain size. The Y_2O_3 itself stays at the grain boundaries as clusters.

2. The presence of zirconium compound dominated the alloys in the form of Zr6Mo6AlTi-xY. The other components were $AlZr_3$, MoO_2, and ZrO_2 oxide.

3. The effect of Y addition into Zr-based alloys was found to be beneficial by shifting the corrosion potential to a more noble value. Zr-6Mo-6Al-Ti-4Y has a higher corrosion potential than the 2 and 3 wt.% Y alloys by a margin of 200 mV. This indicates that the metal is more resistant to corrosion. The increased corrosion resistance of Zr-based alloys was due to the formation of zirconium oxide, titanium oxide, aluminum oxide, molybdenum oxide, and yttrium oxide.

4. However, this appears to have another consequence: The passive region of Zr-6Mo-6Al-Ti-4Y was the shortest among them, as can be seen in the breakdown potential (Eb) values of 0.04 V. It is suggested that the Y addition affects the passivity activity.

Use of AI tools declaration

The authors declare they have not used Artificial Intelligence (AI) tools in the creation of this article.

Conflicts of interest

The data used in this article are originally obtained from the experiment conducted by the authors. All parties that have contributed either to this article or to the experiment have been recognized for their contribution.

References

1. Saini M, Singh Y, Arora P, et al. (2015) Implant biomaterials: A comprehensive review. *World J Clin Cases* 3: 52–57. https://doi.org/10.12998/wjcc.v3.i1.52

2. Guarino V, Iafisco M, Spriano S (2020) Introducing biomaterials for tissue repair and regeneration, In: Guarino V, Iafisco M, Spriano S, *Nanostructured Biomaterials for Regenerative Medicine*, Woodhead Publishing, 1–27. https://doi.org/10.1016/B978-0-08-102594-9.00001-2

3. Niinomi M, Hanawa T, Okazaki Y, et al. (2010) Contributor contact details, In: Niinomi M, *Metals for Biomedical Devices*, London: Woodhead Publishing, xi-xiii. https://doi.org/10.1016/B978-1-84569-434-0.50019-X

4. Tanzi MC, Farè S, Candiani G (2019) Chapter 4-Biomaterials and applications, In: Tanzi MC, Farè S, Candiani G, *Foundations of Biomaterials Engineering*, New York: Academic Press, 199–287. https://doi.org/10.1016/B978-0-08-101034-1.00004-9

5. Hua N, Chen W, Zhang L, et al. (2017) Mechanical properties and bio-tribological behaviors of novel beta-Zr-type Zr-Al-Fe-Nb alloys for biomedical applications. *Mater Sci Eng C* 76: 1154–1165. https://doi.org/10.1016/j.msec.2017.02.146

6. Ratner BD, Hoffman AS, Schoen FJ, et al. (2004) *Biomaterials Science: An Introduction to Materials in Medicine*, Amsterdam: Elsevier.

7. Nie L, Zhan Y, Liu H, et al. (2014) Novel β-type Zr–Mo–Ti alloys for biological hard tissue replacements. *Mater Design* 53: 8–12. https://doi.org/10.1016/j.matdes.2013.07.008

8. Narushima T (2019) 19-New-generation metallic biomaterials, In: Niinomi M, *Metals for Biomedical Devices,* 2 Eds., London: Woodhead Publishing, 495–521. https://doi.org/10.1016/B978-0-08-102666-3.00019-5

9. Kunčická L, Kocich R, Lowe TC (2017) Advances in metals and alloys for joint replacement. *Prog Mater Sci* 88: 232–280. https://doi.org/10.1016/j.pmatsci.2017.04.002

10. Juliano H, Gapsari F, Izzuddin H, et al. (2022) HA/ZrO$_2$ coating on CoCr alloy using flame thermal spray. *Evergreen* 2: 254–261. https://doi.org/10.5109/4793632

11. Chen Q, Thouas GA (2015) Metallic implant biomaterials. *Mater Sci Eng R Rep* 87: 1–57. https://doi.org/10.1016/j.mser.2014.10.001

12. Moztarzadeh A (2017) Biocompatibility of implantable materialsfocused on titanium dental implants. http://hdl.handle.net/20.500.11956/93643.

13. Yin L, Nakanishi Y, Alao AR, et al. (2017) A review of engineered zirconia surfaces in biomedical applications. *Procedia CIRP* 65: 284–290. https://doi.org/10.1016/j.procir.2017.04.057

14. Grech J, Antunes E (2019) Zirconia in dental prosthetics: A literature review. *J Mater Res Technol* 8: 4956–4964. https://doi.org/10.1016/j.jmrt.2019.06.043

15. Zhou FY, Wang BL, Qiu KJ, et al. (2013) Microstructure, mechanical property, corrosion behavior, and in vitro biocompatibility of Zr–Mo alloys. *J Biomed Mater Res B* 101: 237–246. https://doi.org/10.1002/jbm.b.32833

16. Kondo R, Nomura N, Suyalatu, et al. (2011) Microstructure and mechanical properties of as-cast Zr–Nb alloys. *Acta Biomater* 7: 4278–4284. https://doi.org/10.1016/j.actbio.2011.07.020

17. Cai S, Daymond MR, Khan AK, et al. (2009) Elastic and plastic properties of βZr at room temperature. *J Nucl Mater* 393: 67–76. https://doi.org/10.1016/j.jnucmat.2009.05.007

18. Eliaz N (2019) Corrosion of metallic biomaterials: A review. *Materials* 12: 407. https://doi.org/10.3390/ma12030407

19. Sah AP, Ready JE (2007) Use of oxidized zirconium hemiarthroplasty in hip fractures: Clinical results and spectrum analysis. *J Arthroplasty* 22: 1174–1180. https://doi.org/10.1016/j.arth.2006.10.018

20. Ries MD, Salehi A, Widding K, et al. (2002) Polyethylene wear performance of oxidized zirconium and cobalt-chromium knee components under abrasive conditions. *J Bone Joint Surg* 84: 129–135. https://doi.org/10.2106/00004623-200200002-00018

21. Li C, Zhan Y, Jiang W (2011) Zr–Si biomaterials with high strength and low elastic modulus. *Mater Design* 32: 4598–4602. https://doi.org/10.1016/j.matdes.2011.03.072

22. Nomura N, Tanaka Y, Kondo R, et al. (2009) Effects of phase constitution of Zr-Nb alloys on their magnetic susceptibilities. *Mater Trans* 50: 2466–2472. https://doi.org/10.2320/matertrans.M2009187

23. Batchelor AW, Chandrasekaran M (2004) Implantation and physiological responses to biomaterials, In: Batchelor AW, Chandrasekaran M, *Service Characteristics of Biomedical Materials and Implants*, Singapore: World Scientific Publishing, 23–60. https://doi.org/10.1142/9781860945366_0003

24. Suyalatu, Nomura N, Oya K, et al. (2010) Microstructure and magnetic susceptibility of as-cast Zr–Mo alloys. *Acta Biomater* 6: 1033–1038. https://doi.org/10.1016/j.actbio.2009.09.013

25. Liang JS, Liu LB, Xu GL, et al. (2017) Compositional screening of Zr-Nb-Mo alloys with CALPHAD-type model for promising bio-medical implants. *Calphad* 56: 196–206. https://doi.org/10.1016/j.calphad.2017.01.001

26. Northwood DO (1978) Heat treatment, transformation reactions and mechanical properties of two high strength zirconium alloys. *J Less Common Met* 61: 199–212. https://doi.org/10.1016/0022-5088(78)90215-1

27. Zhou FY, Wang BL, Qiu KJ, et al. (2012) Microstructure, corrosion behavior and cytotoxicity of Zr–Nb alloys for biomedical application. *Mater Sci Eng C* 32: 851–857. https://doi.org/10.1016/j.msec.2012.02.002

28. Tewari R, Srivastava D, Dey GK, et al. (2008) Microstructural evolution in zirconium based alloys. *J Nucl Mater* 383: 153–171. https://doi.org/10.1016/j.jnucmat.2008.08.041

29. Zhang X, Zhang B, Liu SG, et al. (2020) Microstructure and mechanical properties of novel Zr–Al–V alloys processed by hot rolling. *Intermetallics* 116: 106639. https://doi.org/10.1016/j.intermet.2019.106639

30. Chelariu R, Trinca LC, Munteanu C, et al. (2017) Corrosion behavior of new quaternary ZrNbTiAl alloys in simulated physiological solution using electrochemical techniques and surface analysis methods. *Electrochimica Acta* 248: 368–375. https://doi.org/10.1016/j.electacta.2017.07.157

31. Xia J, Ren K, Wang Y (2019) Reversible joining of zirconia to titanium alloy. *Ceram Int* 45: 2509–2515. https://doi.org/10.1016/j.ceramint.2018.10.180

32. Zhou K, Liu Y, Pang S, et al (2016) Formation and properties of centimeter-size Zr–Ti–Cu–Al–Y bulk metallic glasses as potential biomaterials. *J Alloy Compd* 656: 389–394. https://doi.org/10.1016/j.jallcom.2015.09.254

33. Huang L, Qiao D, Green BA, et al. (2009) Bio-corrosion study on zirconium-based bulk-metallic glasses. *Intermetallics* 17: 195–199. https://doi.org/10.1016/j.intermet.2008.07.020

34. Zhao X, Niinomi M, Nakai M, et al. (2011) Development of high Zr-containing Ti-based alloys with low Young's modulus for use in removable implants. *Mater Sci Eng C* 31: 1436–1444. https://doi.org/10.1016/j.msec.2011.05.013

35. Wang ZM, Ma YT, Zhang J, et al. (2008) Influence of yttrium as a minority alloying element on the corrosion behavior in Fe-based bulk metallic glasses. *Electrochimica Acta* 54: 261–269. https://doi.org/10.1016/j.electacta.2008.08.017

36. Toby BH, Von Dreele RB (2013) GSAS-II: the genesis of a modern open-source all purpose crystallography software package. *J Appl Crystallogr* 46: 544–549. https://doi.org/10.1107/S0021889813003531

37. Akimoto T, Ueno T, Tsutsumi Y, et al. (2018) Evaluation of corrosion resistance of implant-use Ti-Zr binary alloys with a range of compositions. *J Biomed Mater Res B* 106: 73–79. https://doi.org/10.1002/jbm.b.33811

38. Yu L, Tang J, Qiao J, et al. (2017) Effect of Yttrium addition on corrosion resistance of Zr-based bulk metallic glasses in NaCl solution. *Int J Electrochem Sc* 12: 6506–6519. https://doi.org/10.20964/2017.07.47